

Engineering Interfaces to Steer Hole Dynamics of BiVO₄ Photoanodes for Solar Water Oxidation

Xiaoyong Xu,* Sen Jin, Chi Yang, Jing Pan, Wei Du, Jingguo Hu,* Haibo Zeng,* and Yong Zhou*

Solar-driven photo-electrochemical (PEC) water splitting paves a promising route toward the future of scalable hydrogen production. However, water oxidation dominated by hole carriers excited in the photoanode is a critical bottleneck that hampers PEC overall efficiency due to sluggish hole transfers and surface reaction kinetics for most semiconductors. Herein, dual interface layers including a buried p–n junction and an active catalytic surface to synergistically accelerate hole extraction and injection toward water oxidation over n-type BiVO₄ photoanodes by successive deposition of discrete p-type Co₃O₄ and amorphous Co-Fe-layered double hydroxide (CoFe-LDH) are introduced. Compared with the bare BiVO₄ photoanode, the resultant BiVO₄/Co₃O₄/CoFe-LDH photoanode yields a near fourfold enhanced photocurrent density of 3.9 mA cm⁻² at 1.23 V_{RHE} with a cathodic shift of ≈410 mV at onset potential under AM 1.5G illumination. Stoichiometric oxygen and hydrogen generation with a Faraday efficiency of unity over 10 h enable an outstanding applied bias solar-to-hydrogen efficiency of 1.23%, among the best records for reported single-photon photoanodes. Furthermore, the decoupled dynamics analysis determines that the designed dual interfaces contribute to both hole extraction efficiency of up to 90% and a surface injection efficiency of up to 71%. This work describes an effective strategy of interface engineering to steer hole dynamics in solar fuel conversion devices.

2H₂O + 4h⁺ → O₂ + 4H⁺) on photoanodes.^[3] However, the four-hole-accepted (i.e., four-electron-donated) WOR is an uphill reaction thermodynamically with high activation energy and requires a large overpotential to compete.^[4] Thus the photoanodes must enable thermodynamically active hole migration to the surface (solid–electrolyte interface, SEI) to cultivate a highly oxidizing environment. Unfortunately, most narrow band-gap semiconductors that are responsive to visible light, such as tantalum nitride (Ta₃N₅)^[5,6] and bismuth vanadate (BiVO₄)^[7,8] suffer from poor charge (especially holes) transport and sluggish surface WOR kinetics; moreover, they are generally prone to photocorrosion in the highly oxidative environment of water oxidation. Therefore, the development of efficient and robust photoanodes is of crucial significance for PEC water splitting but also very challenging.^[9]

The n-type BiVO₄ (BVO) has been considered as one of the most promising photoanodes for cost-effective PEC water-

splitting cells because it has a desirable band alignment that allows the substantial absorption of solar spectrum and endows enough thermodynamic potential for water splitting.^[10–12] However, the solar-to-hydrogen (STH) conversion efficiency achieved with BVO to date has been far below the theoretical value (≈9.2%) due to poor bulk charge transport and surface reaction kinetics.^[13–15] Integrating with WOR cocatalysts (WOCs) has been shown as an effective approach of

1. Introduction

Photo-electrochemical (PEC) water splitting for hydrogen (H₂) production by using semiconductors to absorb sunlight offers a promising strategy toward the future green and renewable energy demands.^[1,2] In order to maintain PEC water reduction for evolving H₂ on photocathodes, the consumed protons must be compensated by water-oxidation reaction (WOR,

Dr. X. Xu, Dr. S. Jin, Dr. J. Pan, Dr. W. Du, Prof. J. Hu
College of Physics Science and Technology
Yangzhou University
Yangzhou 225002, China
E-mail: xxy@yzu.edu.cn; jghu@yzu.edu.cn

Dr. X. Xu, Prof. H. Zeng
Institute of Optoelectronics and Nanomaterials
College of Materials Science and Engineering
Nanjing University of Science and Technology
Nanjing 210094, China
E-mail: zeng.haibo@njust.edu.cn

Dr. W. Du, Prof. Y. Zhou
School of Physics
Nanjing University
Nanjing 210093, China
E-mail: zhouyong1999@nju.edu.cn

Prof. C. Yang
Yale-NUIST Center on Atmospheric Environment
International Joint Laboratory on Climate and Environment Change (ILCEC)
Nanjing University of Information Science & Technology
Nanjing 210044, China

 The ORCID identification number(s) for the author(s) of this article can be found under <https://doi.org/10.1002/solr.201900115>.

DOI: 10.1002/solr.201900115

improving surface reaction kinetics to assist hole extraction and injection against charge recombination.^[16,17] However, the semiconductor–cocatalyst interface (SCI) may introduce more surface-trapped states as charge recombination centers or oxidative corrosion sites, instead of deteriorating PEC performance.^[18] In addition, the turnover frequency (TOF) of water oxidation at any WOCs is generally less than the hole-arrival frequency (HAF) at SCI, and then the accumulation of SCI-reaching holes instead loses a portion to additional surface recombination or adverse oxidation.^[19,20] Therefore, only loading WOCs is not enough to optimum hole dynamics for solar water oxidation.^[21,22] Kim et al.^[18] have noticed the interface states at the BVO–WOC interface with increased charge recombination and creatively applied dual layers of WOCs that can simultaneously reduce charge recombination at SCIs and accelerate hole injection at SEIs, enabling the well-steered hole dynamics into water oxidation. Liu et al.^[23] have introduced the concept of hole-storage layers (HSLs) using ferrihydrite between Ta₃N₅ and WOC to transfer and store holes, allowing sustainable water oxidation at the otherwise unstable Ta₃N₅ photoanode. Recently, Chang et al.^[24] loaded p-type Co₃O₄ cocatalysts onto n-type BVO photoanodes, which not only optimizes surface reaction kinetics but also forms p–n junctions with a built-in electric field to facilitate charge separation. Note that the crystallized p-type Co₃O₄ cannot actually tolerate the agglomeration of energetic holes from the valence states of BVO, and especially the endurance of photoanodes with p-type Co₃O₄ as the outermost layer in harsh oxidative environments needs to be carefully examined. Hence, developing an effective strategy of controlling hole dynamics toward water oxidation is crucially important to design robust photoanodes of PEC water splitting.

Herein, to this end, we designed the dual interfaces to simultaneously boost hole extraction and injection toward WOR through the serial deposition of p-type Co₃O₄ and Co-Fe-layered double hydroxide (CoFe-LDH) over the BVO photoanode, enabling an optimized utilization of photogenerated holes for

solar water oxidation. The resultant BVO/Co₃O₄/CoFe-LDH (BCCF-H) photoanode achieves a high photocurrent density of 3.91 mA cm⁻² at 1.23 V_{RHE} under 1 sun irradiation (AM 1.5G, 100 mW cm⁻²) and warrants a record applied bias solar-to-hydrogen (AB-STH) efficiency of 1.23%. Two efficiencies of hole extraction and injection catalysis were probed by the dynamics decoupling method, illuminating the benefits of two functional interfaces in steering holes to instigate water oxidation.

2. Results and Discussions

2.1. Design and Construction

Figure 1 shows the schematic overview of the synthesis process of the BCCF-H electrode in this work (see the Experimental Section for details). In brief, the porous BVO electrodes were first prepared through electrochemical deposition of BiOI nanosheets (NSs) onto a fluorine-doped tin oxide (FTO) substrate and then annealing with a vanadium precursor [VO(acac)₂] onto their surface; the subsequent loading of Co₃O₄ nanoparticles (NPs) and CoFe-LDH NSs was serially carried out via in situ photo- and electro-deposition methods. The scanning electron microscopy (SEM) images of the products in the synthesis process are shown in Figure 1a–d. The deposited BiOI on FTO appears as a mesh-shaped structure comprising vertically standing 2D thin NSs (Figure 1a), in which the formed voids inhibit grain growth of the BVO during the annealing conversion process. The porous BVO is composed of tightly connected worm-like particles with amounts of cavities in sizes of 400–500 nm (Figure 1b). Such a 3D nanoporous network that creates a high-specific surface area service for electrolyte penetration and gas product overflow has been recognized as the favorable architecture for PEC electrodes.^[25] More importantly, the mean particle size of the BVO-constructing porous electrode is around 80 nm, which coincides well with the particle size estimated by X-ray diffraction (XRD) data using the Scherrer equation (Figure S1, Supporting

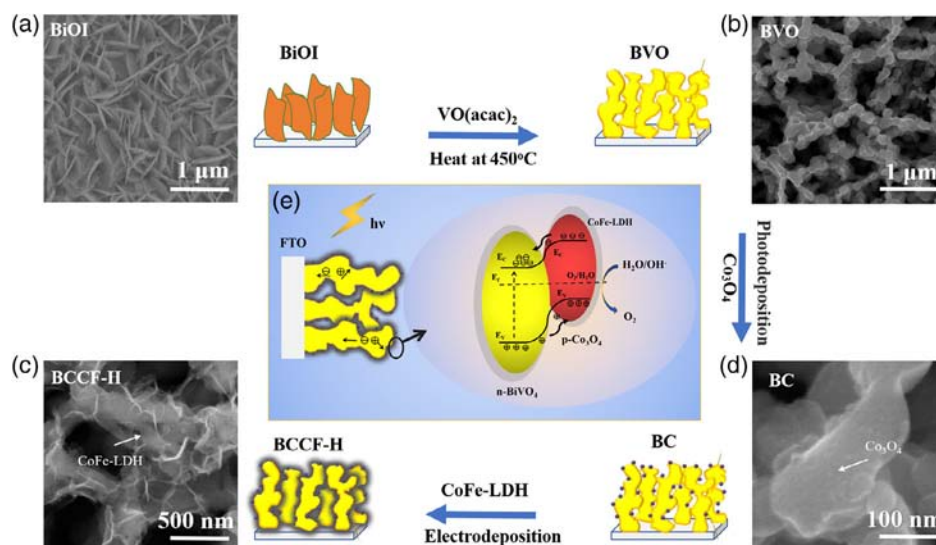


Figure 1. Schematic of the synthetic route of the BCCF-H electrode, with SEM images of a) BiOI b) BVO c) BC, and d) BCCF-H. e) Photogenerated hole dynamics mechanism proposed in BCCF-H for PEC water oxidation.

Information), and the relatively smaller particle size than hole-diffusion length ($L_D \sim 100$ nm)^[26] in the BVO crystal reinforces the propensity of photogenerated holes reaching the surface under the built-in electric field in the space charge region. After the loading of Co_3O_4 , the porous BVO is uniformly decorated with densely dispersed Co_3O_4 NPs of 10–12 nm in size on the surface (Figure 1c), further evidenced by transmission electron microscopy (TEM) and high-resolution TEM (HRTEM) images (Figure S2, Supporting Information). The p-type Co_3O_4 can form a p-n junction with the underlying n-type BVO to accelerate charge separation; meanwhile, CoO_x is also an effective WOC. Chang et al.^[24] deposited p- Co_3O_4 onto n-BVO photoanodes to describe the simultaneous enhancement of surface WOR kinetics and bulk charge separation, whereas there was no validation for PEC stability. However, the p- Co_3O_4 crystal actually cannot withstand the agglomeration of highly oxidative holes from BVO, as confirmed by detail experimental tests in the following content, and thus its anodic corrosion hinders the use of p- Co_3O_4 as the outermost cocatalyst for sustainable PEC water oxidation. To address this problem, surface deposition of an active CoFe-LDH WOC over the BVO/ Co_3O_4 (BC) electrode was employed as a feasible approach. The resultant BCCF-H composite shows that the ultrathin CoFe-LDH NSs wrap uniformly the whole skeleton, maintaining the 3D porous structure (Figure 1d). Note that the bimetallic (BM) LDHs have been identified as a class of highly active WOR catalysts due to their versatile composition and abundant active sites.^[27,28] Moreover, the optical transparency of their ultrathin NSs has enabled the integration with semiconductor photoanodes to promote PEC water oxidation.^[15,29] Here the CoFe-LDH catalyst with a deposition time of 80 s is an optimum selection for superior electrocatalytic activity and optical transparency (Figure S3, Supporting Information). We also

deposited the single Co_3O_4 or CoFe-LDH on the porous BVO to fabricate the BC and BVO/CoFe-LDH (BCF-H) electrodes for comparison studies. The loading mass of Co_3O_4 and CoFe-LDH could be successively adjusted by their deposition time and be optimized so as to maximize photocurrent generation (Figure S4, Supporting Information). In a word, the discrete p-type Co_3O_4 NPs deposited on the porous BVO surface create abundant p-n junctions buried at SCIs for enhanced charge separation (i.e., hole extraction); the in situ-formed CoFe-LDH shell as the new SEI shields Co_3O_4 against corrosion while operating faster WOR (i.e., hole injection), as illustrated by the photogenerated hole dynamics mechanism depicted in Figure 1e.

Figure 2 presents the characterization on morphology and the microstructure of the resultant BCCF-H composite electrode. The SEM image (Figure 2a) shows that the ultrathin CoFe-LDH NSs were vertically supported on the nanoporous skeleton, forming the interconnected nanowall as an outermost shell. The cross-sectional SEM image (Figure S5, Supporting Information) reveals the uniformly porous texture of the BCCF-H film ≈ 1.2 μm in thickness. The TEM image (Figure 2b) further reveals the ultrathin nature (electron beam transparent) of CoFe-LDH NSs and their outermost positions. Energy-dispersive X-ray spectroscopy (EDS) elemental mappings (Figure 2c) clearly show the central body distribution of Bi and V elements and the homogeneous whole distribution of O, Co and Fe elements, verifying further the shell–core structure of the BCCF-H composite. The HRTEM image in Figure 2d shows the interface microstructure, where the inner BVO presents the well-defined lattice fringes of the (–121) plane with a spacing of 0.311 nm whereas the outer CoFe-LDH (red dashed box) appears to be of amorphous texture without lattice fringes, and at their interface region (yellow dashed box), the local lattice fringes of the Co_3O_4 (311) plane are revealed to intersect with

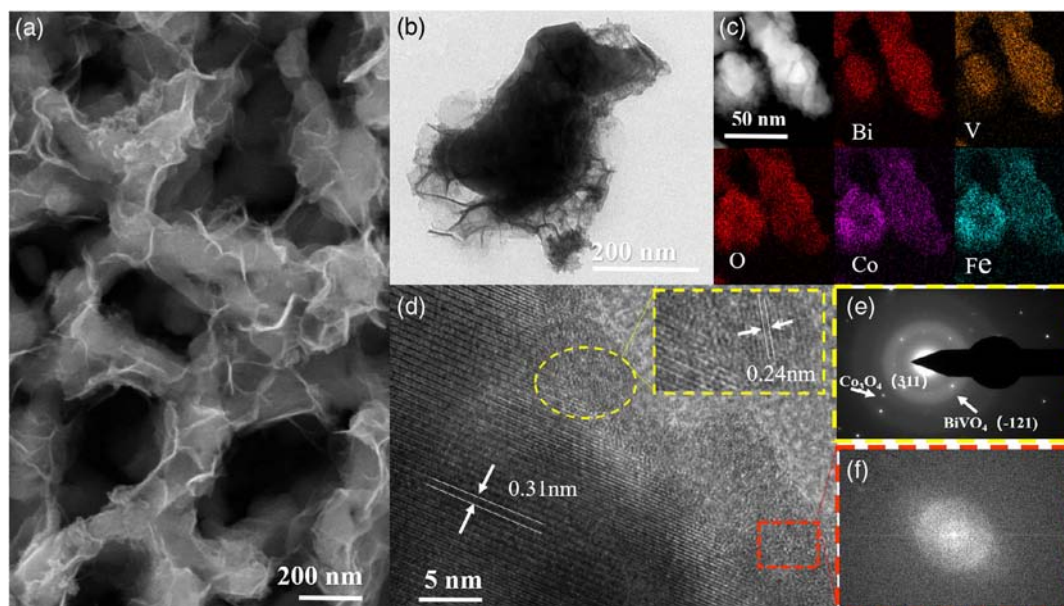


Figure 2. a) SEM images of the resultant BCCF-H electrode. b) TEM image of the BCCF-H composite with c) EDS elemental mapping for Bi, V, O, Co, and Fe elements. d) The HRTEM image of the BCCF-H composite with e,f) SAED patterns on its interface (yellow dashed box) and shell (red dashed box) regions.

that of BVO. The corresponding selected-area electron diffraction (SAED) patterns also evidence the heterogeneous (Figure 2e) and amorphous (Figure 2f) natures in two different regions, respectively. These results identify the clear hierarchical assembly of the shell–core structure with heterojunctions buried at interfaces. Note that the vertically standing nanowalls constructed with ultrathin and amorphous CoFe-LDH NSs can not only expose a large surface area for catalytic reactions but also ensure optical transparency to avoid light-harvesting loss, promising to be a desirable architecture for loading cocatalysts.^[29]

2.2. Photo-Electrochemical Performance

In order to test the effect of Co_3O_4 modification, we first investigated the PEC performance of pristine BVO and composited BC photoanodes in 0.5 M KPi aqueous solution for water oxidation (without Na_2SO_3) and sulfite oxidation (with 1 M Na_2SO_3 as a hole scavenger) in terms of linear sweep voltammetry (LSV) and chronoamperometry ($j-t$) scans. As shown in Figure 3a, the BC photoanode yields water-oxidation photocurrent density of up to 2.98 mA cm^{-2} at $1.23 \text{ V}_{\text{RHE}}$ under 1 sun irradiation, which is near three times that of the pristine BVO counterpart; moreover, the LSV curves of the BC electrode display noticeable cathodic shifts in onset potentials compared with the BVO electrode whether in dark conditions or under illumination, indicating the improved WOR kinetics by laden Co_3O_4 . Whereas for sulfite oxidation, with equally fast oxidation kinetics (Figure 3b), no obvious shift is observed on the dark LSV curves between BC and BVO electrodes; however the BC electrode exhibits an earlier

photocurrent onset and generates higher photocurrent density than BVO electrode in the whole potential window, which suggests more negative flatband potential (E_{fb}) and more efficient hole extraction in the BC electrode after integrating with p-type Co_3O_4 . Thereby, the discrete p-type Co_3O_4 is reasonably assumed to form abundant p-n junctions with the underlying n-type BVO, which builds outward electric fields driving charge separation (i.e., hole extraction); meanwhile, they also serve as effective WOCs in improving surface reaction kinetics. However, the continuous LSV scans (Figure 3c) reveal a gradual decay of the photocurrent density of the BC electrode for water oxidation, and after the 50th scan the PEC behavior is close to that of the pristine BVO. The rapid PEC-performance decay of the BC electrode toward a low level of the BVO electrode is also evidenced by $j-t$ measurements (Figure 3d), along with the color change from dark yellow to bright yellow (Figure S6, Supporting Information). The tested BC electrode after the long-term $j-t$ measurement is discovered to be missing Co species from the surface, as evidenced by the SEM image and the corresponding EDS spectrum (Figure S7, Supporting Information). Whereas the BC photoanode can maintain good stability for sulfite oxidation (red dashed line in Figure 3d). Thus the poor photostability of the BC photoanode is demonstrated to be most likely due to the dissolution of Co_3O_4 upon accumulation of holes excited on BVO, making Co_3O_4 impossible to warrant its multiple roles as the outermost layer. In addition, it should be noted that the increased photocurrent of the BC electrode may include the contribution of Co species reaction rather than only arising from water oxidation. Thus we further deposited the ultrathin CoFe-LDH NSs over the BC

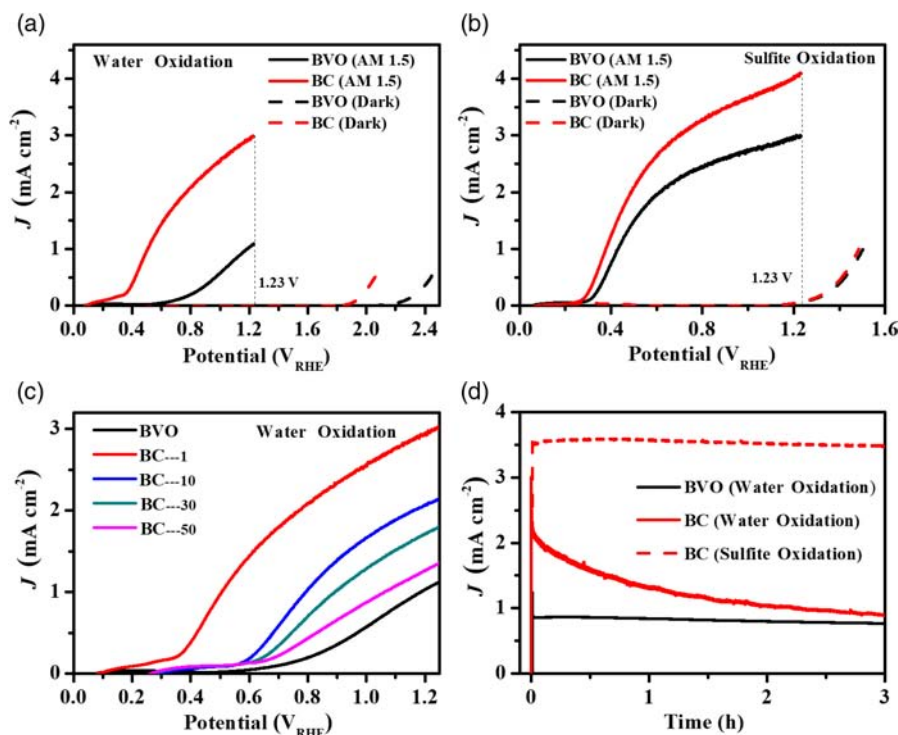


Figure 3. LSV curves of BC and BVO photoanodes in the dark and under AM 1.5G illumination in 0.5 M KPi solution (pH = 7) a) without and b) with 1 M Na_2SO_3 . c) Repeated LSV curves of BC photoanodes from the first to the 50th scans under AM 1.5G illumination without 1 M Na_2SO_3 . d) $j-t$ curves at $1.23 \text{ V}_{\text{RHE}}$ under AM 1.5G illumination of BVO and BC photoanodes without/with 1 M Na_2SO_3 .

electrode to create a more robust WOC shell, and then the PEC performances of the sustainable BVO, BCF-H, and BCCF-H electrodes were comparatively investigated apart from the unstable BC electrode.

The PEC properties of BCF-H, BCCF-H, and BVO photoanodes for water oxidation and sulfite oxidation with/without AM 1.5G illumination were investigated. The dark LSV curves for water oxidation (Figure 4a) reveal the significantly cathodic shift of onset potentials after loading CoFe-LDH, which suggests the excellent cocatalytic effect of CoFe-LDH toward WOR, and the earliest onset that occurred at BCCF-H can be attributed to the most negative E_{fb} mediated by p-type Co_3O_4 , as evidenced by their Mott-Schottky plots (Figure S8, Supporting Information). For accessible sulfite oxidation (Figure 4b), the three photoanodes exhibit similar dark LSV curves insensitive to kinetic and thermodynamic modulation. For water oxidation under AM 1.5G illumination (Figure 4c), the ternary BCCF-H electrode yields the significantly enhanced water-oxidation photocurrent generation, and specifically the photocurrent densities

at $1.23 V_{RHE}$ sequentially rise to 3.91 from 1.09 mA cm^{-2} for the pristine BVO electrode and 2.64 mA cm^{-2} for the BCF-H electrode. The improved WOR kinetics by the CoFe-LDH cocatalyst can be further evidenced by the earlier onset of water oxidation after loading CoFe-LDH NSs. Notably, when compared with the BCF-H electrode, the improvement of water-oxidation photocurrent density for the BCCF-H electrode is found to be partly benefited from the p-type Co_3O_4 existence, indicating enhanced photogenerated charge separation, owing to the buried p-n junctions. Furthermore, when unifying the surface catalytic reaction kinetics by sulfite oxidation, the improved photocurrent output upon p-type Co_3O_4 clearly confirms the charge separation effect across the p-n junction interface. Whereas, the slightly decreased sulfite-oxidation photocurrent generation for BVO upon the loading of only CoFe-LDH reveals the decrement of surface-reaching holes due to the introduction of additional SCI, implying the demand for charge separation acceleration via p-n junctions at the SCI. Through comparison on the above PEC performances, our porous BVO electrode fails mainly at poor water-oxidation

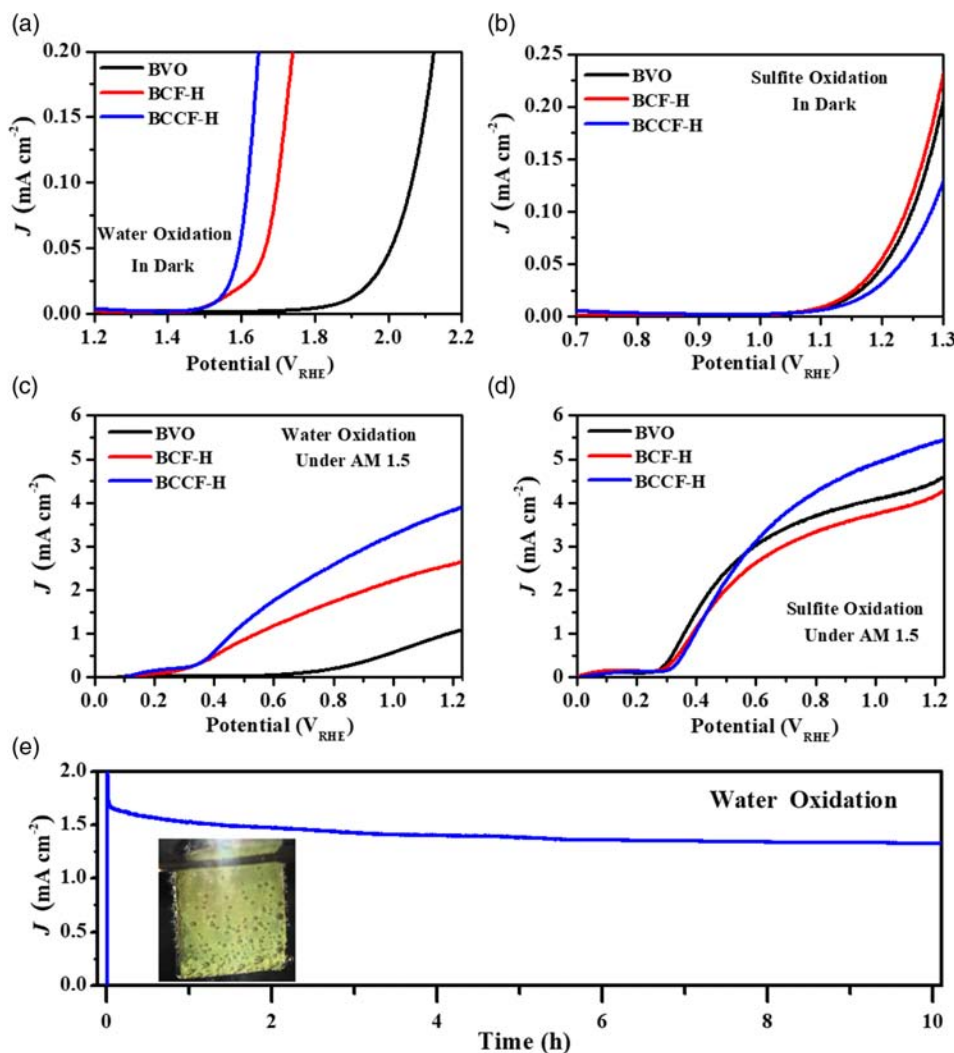


Figure 4. LSV curves of BCF-H, BCCF-H, and BVO photoanodes a,b) in dark and c,d) under illumination for a,c) water oxidation and b,d) sulfite oxidation (with $1 \text{ M Na}_2\text{SO}_3$). e) $j-t$ curve of the BCCF-H photoanode with its photograph (inset) for water oxidation at $0.6 V_{RHE}$ under illumination.

kinetics on the BVO surface rather than hole-extraction dynamics or charge recombination loss. When loading CoFe-LDH NSs as WOCs on the BVO to improve water-oxidation kinetics, the formed SCI instead damages the hole-outflow capacity because of the charge recombination rate increasing at additional SCI states. Thus, the p-type Co_3O_4 NPs were buried at the SCI interface to create abundant p-n junctions as charge separation actuators for diminishing interface recombination loss.

The PEC stability of the BCCF-H electrode using the water-oxidation photoanode was examined by the long-term $j-t$ measurement at $0.6 V_{\text{RHE}}$. As shown in Figure 4e, the photocurrent density of the BCCF-H photoanode is almost constant and maintains around 93% of the initial value even after 10 h of continuous operation. The vigorous effervescence with O_2 bubbles during the whole stability testing process, observable by the

naked eye (see the inset in Figure 4e), promises the robust activity of the BCCF-H photoanode for PEC water-oxidation applications. Furthermore, the SEM and EDS analyses after stability testing indicate no noticeable change in morphology and composition (Figure S9, Supporting Information), further confirming the good durability of the BCCF-H photoanode during the PEC water-oxidation process.

2.3. Quantum Dynamics

Along with PEC stability testing for the BCCF-H electrode, the evolved O_2 and H_2 gases were quantified by gas chromatography (GC) integration and compared with the theoretical amounts calculated from the photocurrent data (see the Experimental Section for details). As shown in Figure 5a, the stoichiometric evolution

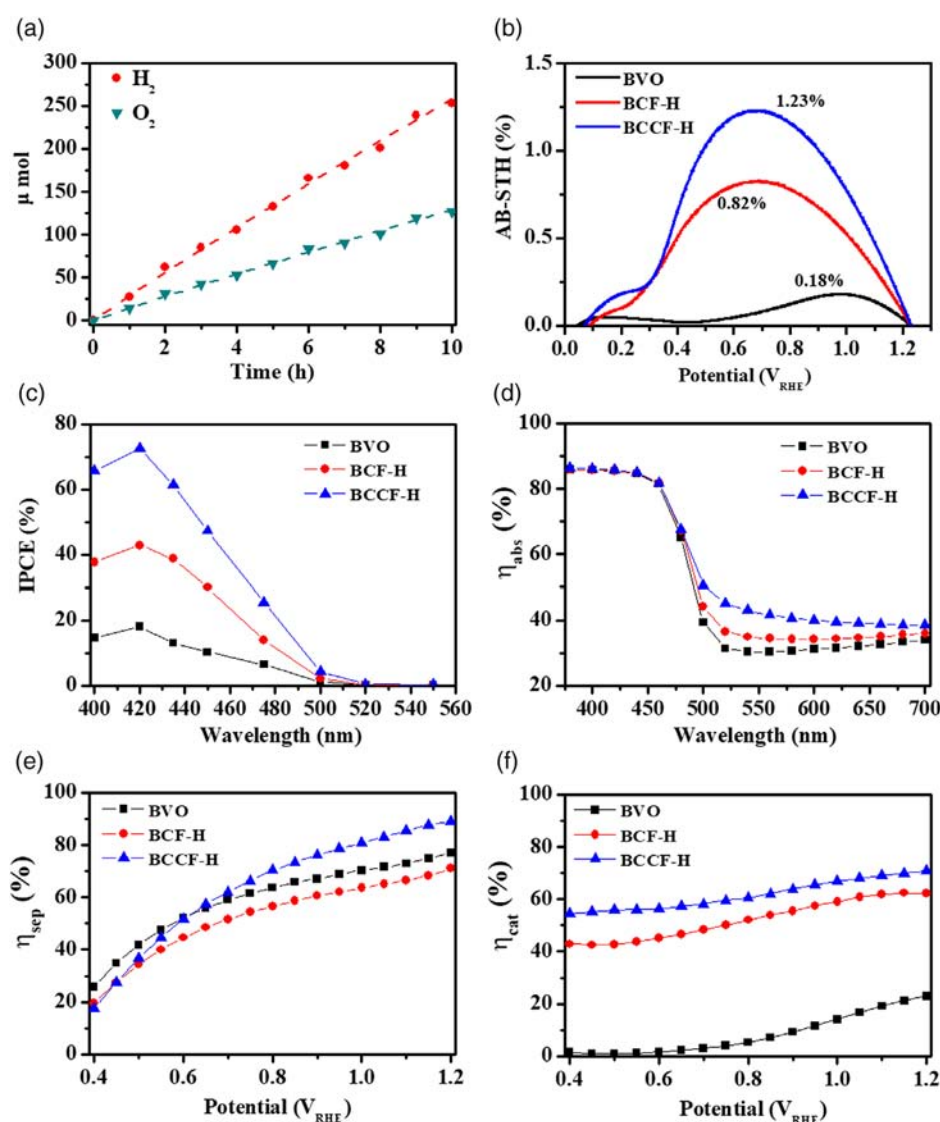


Figure 5. a) Amounts of H_2 and O_2 evolution from the BCCF-H photoanode and Pt counter electrode at $0.6 V_{\text{RHE}}$; dashed curves indicate theoretical amounts of H_2 and O_2 evolution calculated based on photocurrent densities with 100% Faraday efficiency. b) AB-STH efficiencies and c) IPCE spectra of BVO, BCF-H, and BCCF-H photoanodes, and their photoexcited quantum dynamics efficiencies: d) photon absorption, e) charge separation, and f) surface catalysis.

of H₂ and O₂ with a ratio of virtually 2 is demonstrated and their amounts are close to the photocurrent-based theoretical values with Faraday efficiency of unity. Such fine correspondence confirms the photocurrent through the PEC cell derives from water splitting, and thus the AB-STH efficiencies can be calculated using the measured LSV data (Figure 5b). The BCCF-H photoanode achieves a maximum AB-STH efficiency up to 1.23%, which is much higher than those of its BCF-H and BVO counterparts and among the best records for the reported single-photon photoanodes (Table S1, Supporting Information). Moreover, this efficiency can be obtained at a potential as low as 0.65 V_{RHE}, enabling a highly favorable feature for assembling tandem cells. Figure 5c shows the wavelength dependence of incident photon-to-current conversion efficiencies (IPCE), where the BCCF-H photoanode exhibits a significant enhancement in the overall optical response range relative to its BVO and BCF-H counterparts, suggesting the superior capacity of photon quantum conversion through BCCF-H for solar water oxidation.

To gain more insights into the photo-induced quantum dynamics, we further quantify the part quantum efficiencies for three dynamic behaviors, photon absorption (η_{abs}), charge separation (i.e., hole extraction, η_{sep}), and surface catalysis (i.e., hole injection, η_{cat}), by using the decoupling analysis method (see the Experimental Section for details). For photon absorption (Figure 5d), the ultrathin CoFe-LDH has little impact on BVO due to its good optical transparency, whereas there is a noticeable η_{abs} growth in BCCF-H over the long wavelength region. Band-gap energies estimated based on UV-vis absorption spectra (Figure S10, Supporting Information) identify that the band-gap transition of Co₃O₄ extends the optical absorption range, which contributes to photon harvesting of the BCCF-H photoanode. Moreover, the photoexcitation of p-type Co₃O₄ is necessary to activate p-n junctions with quasi-Fermi-level splitting for driving photogenerated charge separation (Figure S11, Supporting Information). For charge separation (Figure 5e), the porous BVO electrode itself can reach a high level, such as η_{sep} up to 70% at 1.23 V_{RHE}, indicating that the photogenerated holes tend to reach the electrode surface due to the smaller size of BVO particles than the hole-diffusion length. The bare BVO electrode executes a considerably inefficient surface catalysis (Figure 5f) because of the poor WOR nature on the BVO surface, leading to a huge loss of surface-reaching holes into surface recombination before injection into surface catalysis. The efficiency of surface catalysis can be significantly improved upon by loading of CoFe-LDHs (Figure 5f), while hindering hole diffusion toward the SEI, and thus a slight decrease in bulk charge separation efficiency is seen in Figure 5e. More interestingly, the intervention of p-type Co₃O₄ not only improves the deteriorated charge separation (Figure 5e) through the p-n junctions but also further promotes surface catalytic thermodynamics via enlarging the surface work function.^[30] The decoupling dynamics analysis clearly reveals the roles of each component in the BCCF-H photoanode, which are consistent with the LSV results, which promote together the hole extraction and injection efficiencies up to 90% and 71% at 1.23 V_{RHE}, respectively. In addition, the better charge transfer of the BCCF-H electrode is also demonstrated by electrochemical impedance spectroscopy (EIS) in Figure S12, Supporting Information. The photoluminescence (PL) spectra in Figure S13, Supporting Information, reveal an obvious

fluorescence quenching involved with Co₃O₄, reflecting that the photogenerated electron–hole recombination can be greatly restrained upon the formation of p-n junctions. The open-circuit voltage (V_{oc}) decay experiment was further conducted to probe the photogenerated charge dynamics (Figure S14, Supporting Information), where the prolonged lifetime (τ) of the photogenerated charge with more effective separation in the BCCF-H electrode is further determined when compared with its BCF-H and BVO counterparts.

3. Conclusion

In summary, we demonstrate the important role of the engineering interface played in steering hole dynamics to improve PEC performance. We introduce p-type Co₃O₄ NPs and amorphous CoFe-LDH NSs over the porous BVO photoanode to construct buried p-n junctions and WOC shells as functional semiconductors/cocatalysts and electrode/electrolyte interfaces, which accelerate hole extraction and injection toward WOR, respectively. The optimized BCCF-H photoanode yields an impressive photocurrent density of 3.91 mA cm⁻² at 1.23 V_{RHE} under 1 sun irradiation. The AB-STH efficiency is up to 1.23% and stoichiometric O₂ and H₂ evolution are continuously generated with Faraday efficiency of unity over 10 h. The decoupled dynamics analysis demonstrates the simultaneous enhancement of charge separation and surface catalysis kinetics, owing to the synergistic effects of p-n junctions and WOCs. The strategy described in this work is universally applicable to boost propensity for photogenerated holes to instigate oxidation reactions in other photoanode systems.

4. Experimental Section

Preparation of the BVO Electrode: The porous BVO films supported on the FTO substrate were synthesized by first electrochemically depositing BiOI, followed by annealing with VO(acac)₂, according to the previous report.^[18] First, 0.4 M of KI was dissolved into 50 mL of deionized water with pH adjusted to 1.7 by HNO₃, and then 0.97 g of Bi(NO₃)₃·5H₂O was added and vigorously stirred for 10 min. This solution was mixed with 20 mL of absolute ethanol (100%) containing 0.23 m *p*-benzoquinone. The electrochemical deposition was performed by using a typical three-electrode cell, in which FTO glass substrates (1 × 2 cm) acted as the working electrodes (WE), saturated Ag/AgCl (4 M KCl) as the reference electrode (RE), and platinum (Pt) foil as the counter electrode. Cathodic deposition was carried out a constant voltage of -0.1 V versus Ag/AgCl for 3 min. The BiOI deposited on FTO substrates were rinsed with deionized water and dried at room temperature. Second, 200 μL of dimethyl sulfoxide (DMSO) solution containing 0.2 m vanadyl acetylacetonate (VO(acac)₂) was placed on the surface of the prepared BiOI electrodes, followed by heating at 450 °C for 2 h in a muffle furnace (ramp ingrate 2 °C min⁻¹). The obtained electrodes were immersed in 1 m NaOH solution with gentle stirring for 30 min to remove excess V₂O₅. The resultant pure BVO electrodes were washed with deionized water and dried in ambient air.

Preparation of BC Electrode: The photo-deposition of Co₃O₄ on BVO was performed with Co(NO₃)₂ as the precursor, and NaIO₃ was used as the electron acceptor. A simple way to do it, 0.5 mL of Co(NO₃)₂ (2.0 mg mL⁻¹) solution, was added into 50 mL of deionized water containing 1.33 g of NaIO₃. The as-synthesized BVO electrode was placed in the above suspension and irradiated from a 300 W Xe lamp with a power intensity calibrated to 100 mW cm⁻² for 30 min. The loading mass of Co₃O₄ was adjusted at different deposition times of 30, 60, and 90 min to optimize the

loading effect. After controlled photo-deposition, the electrode was finally rinsed with deionized water and dried at 80 °C in a vacuum oven for 24 h.

Preparation of BCCF-H and BCF-H Electrodes: The electro-deposition of the CoFe-LDH catalysts was further performed over composite BC and pure BVO electrodes to prepare BCCF-H and BCF-H electrodes, respectively. In a typical procedure, 0.08 g of $\text{Co}(\text{NO}_3)_2 \cdot 6\text{H}_2\text{O}$ and 0.12 g of $\text{Fe}(\text{NO}_3)_3 \cdot 9\text{H}_2\text{O}$ were successively dissolved into 50 mL of deionized water to prepare the Co-Fe equimolar electrolyte for the following electro-deposition method. By using a three-electrode electrochemical system with Ag/AgCl as the RE and graphite rod as the counter electrode, pure BVO and composite BC electrodes respectively served as the WEs to execute the electro-deposition of CoFe-LDH catalysts under a constant voltage of -1.0 V versus Ag/AgCl with a varying deposition time from 50 to 320 s. The optimum deposition time was found to be 80 s. Consequently, the obtained BCCF-H and BCF-H electrodes were rinsed with deionized water and dried at room temperature in a vacuum oven.

Structural Characterization: SEM images were obtained on a Hitachi S-4800II field emission scanning electron microscope with an accelerating voltage of 20 kV. TEM and HRTEM were taken on a Tecnai F30 electron microscope equipped with EDX spectroscopy. XRD measurements were conducted on the Shimadzu XRD-7000 diffractometer with Cu K α radiation ($\lambda = 0.154\text{ nm}$). Raman spectra were obtained by a research laser Raman microscope (Renishaw inVia). UV-vis spectroscopy was performed using a Cary 5000 spectrophotometer (Varian). The PL spectra were recorded on an FL4600 spectrophotometer (Hitachi) using Xe lamp emission with regulatory wavelength as the excitation source.

Photo-electrochemical Measurements: All PEC measurements were performed with a standard three-electrode electrochemical workstation (CHI 660E, CH Instrument, Shanghai). The fabricated electrodes acted as the WE, Pt foil as the counter electrode and Ag/AgCl as the RE. The "1 sun" illumination was simulated by a 300 W Xe short arc lamp solar simulator (PerfectLight, Beijing, PLS-SXE 300C) with an AM 1.5G filter. The light intensity was calibrated to 100 mW cm^{-2} at the surface of the photoelectrodes by an irradiatometer (Beijing, FZ-A). Photocurrent measurements were performed in a 0.5 M potassium phosphate (KPI) buffer solution (pH = 7) with or without 1 M sodium sulfite (Na_2SO_3) as a hole scavenger after being purged with N_2 . Photocurrent densities were monitored either using LSVs with a scan rate of 10 mV s^{-1} or using $j-t$ scans at a constant bias of 0 V versus Ag/AgCl. All results in this work were presented against the reversible hydrogen electrode (RHE) according to the potential conversion relationship

$$E_{\text{RHE}} = E_{\text{Ag/AgCl}} + E_{\text{Ag/AgCl}}^* + 0.0591 \times \text{pH} \text{ (V)} \quad (1)$$

where $E_{\text{Ag/AgCl}}^* = 0.1976\text{ V}$ at 25 °C. The amounts of evolved hydrogen and oxygen were measured by an online GC (GC, 9790 II, Fuli) equipped with a thermal conductivity detector (TCD) and an Ar gas carrier while recording the photocurrent retention over the PEC cell at an AB of 0 V versus Ag/AgCl for 10 h. The Faradaic efficiency (ξ_F) was then calculated by comparing the theoretical amounts with the GC-detected amounts of generated hydrogen and oxygen according to the following equation

$$\xi_F (\%) = \frac{M_{\text{O}_2} \times 4 \times N_A}{J \times t \times A \div e} = \frac{M_{\text{H}_2} \times 2 \times N_A}{J \times t \times A \div e} \times 100\% \quad (2)$$

where M_{O_2} and M_{H_2} are the mole amounts of evolved oxygen and hydrogen through GC detection, N_A is Avogadro number, e is electron charge, J is the photocurrent density, t is time, and A is the PEC effective area of the electrode. The EIS measurements were performed in the potentiostatic mode at open-circuit potential by applying an AC voltage amplitude of 5 mV within the frequency range from 10^5 to 10^{-3} Hz. The capacitance measurement on the electrode/electrolyte was employed to determine E_b using Mott-Schottky plots with $1/C_{sc}^2$ versus potential at a fixed frequency of 100 kHz in the dark.

The AB-STH efficiencies were calculated from the LSV curves using the following equation with ξ_F of unity

$$\text{AB-STH} (\%) = \frac{J \times (E_{\text{OER}} - E_{\text{RHE}}) \times \xi_F}{P_{\text{AM1.5}}} \times 100\% \quad (3)$$

where $P_{\text{AM1.5}}$ is 1 sun energy flux simulated by the AM 1.5G filter and E_{OER} and E_{RHE} are the standard equilibrium potentials of oxygen evolution and the applied potential, respectively.

The IPCEs were evaluated based on the measured photocurrent densities with several single band-pass filters for 400, 420, 435, 450, 475, 500, 520, and 550 nm ($\pm 15\text{ nm}$) through the following derivation

$$\text{IPCE} (\%) = \frac{1240 \times j}{P_{\text{light}} \times \lambda} \times 100\% \quad (4)$$

where 1240 represents a multiplication of Planck's constant (h) and the light speed (c), j is the photocurrent density, λ is the incident light wavelength, and P_{light} is the irradiation power density, respectively.

The quantum efficiencies of three dynamics behaviors were calculated as follows: the photon absorption efficiency (η_{abs}) at each wavelength was estimated from UV-vis absorption spectra using the following equations

$$\eta_{\text{abs}} = 1 - 10^{-A(\lambda)} \quad (5)$$

where $A(\lambda)$ is the absorbance at a certain wavelength. The photon absorption rate can be converted to the theoretical current density (j_{abs}) when assuming absorbed photon-to-current efficiency (APCE) of 100% by using a trapezoidal integration (in 10 nm increments) of the solar energy spectrum in terms of the photon number ($\text{s}^{-1}\text{ m}^{-2}\text{ nm}^{-1}$) versus wavelength (nm).^[18] Thus the measured photocurrent densities arising from PEC performance (j_{PEC}) can be expressed as follows

$$j_{\text{PEC}} = j_{\text{abs}} \times \eta_{\text{sep}} \times \eta_{\text{cat}} \quad (6)$$

The addition of 1 M Na_2SO_3 as a hole scavenger into the electrolyte instigated extremely fast surface oxidation kinetics, i.e., $\eta_{\text{cata}} = 1$, which was assumed to completely suppress surface charge recombination without affecting bulk charge separation. So, the photocurrent densities for PEC sulfite oxidation (j_{sulfite}) and for water oxidation (j_{water}) were expressed as follows, respectively

$$j_{\text{sulfite}} = j_{\text{abs}} \times \eta_{\text{sep}} \quad (7)$$

$$j_{\text{water}} = j_{\text{sulfite}} \times \eta_{\text{cat}} \quad (8)$$

Then, η_{sep} and η_{cat} for PEC water oxidation can be estimated as the ratios of different j_{PEC} values

$$\eta_{\text{sep}} = j_{\text{sulfite}}/j_{\text{abs}} \quad (9)$$

$$\eta_{\text{cat}} = j_{\text{water}}/j_{\text{sulfite}} \quad (10)$$

Supporting Information

Supporting Information is available from the Wiley Online Library or from the author.

Acknowledgements

This work was supported by the National Natural Science Foundation of China (Nos. 11574263, 11374253 and 11774302), the Open Research Fund of Key Laboratory of Advanced Displaying Materials and Devices of Nanjing University of Science and Technology, the Qing Lan Project of Jiangsu Province, and the Advanced Talent Development Plan of Yangzhou University. The authors thank the Testing Centers of Yangzhou University and Nanjing University for their technical support.

Conflict of Interest

The authors declare no conflict of interest.

Keywords

bismuth vanadate, hole dynamics, interface engineering, photoanodes, solar water splitting

Received: March 29, 2019

Revised: July 3, 2019

Published online:

-
- [1] A. Fujishima, K. Honda, *Nature* **1972**, 238, 37.
- [2] M. G. Walter, E. L. Warren, J. R. McKone, S. W. Boettcher, Q. Mi, E. A. Santori, N. S. Lewis, *Chem. Rev.* **2010**, 110, 6446.
- [3] Y. B. Kuang, T. Yamada, K. Domen, *Joule* **2017**, 1, 290.
- [4] C. Ding, J. Shi, Z. Wang, C. Li, *ACS Catal.* **2017**, 7, 675.
- [5] M. Li, W. Luo, D. Cao, X. Zhao, Z. Li, T. Yu, Z. Zou, *Angew. Chem., Int. Ed.* **2013**, 52, 11016.
- [6] Y. Li, T. Takata, D. Cha, K. Takanabe, T. Minegishi, J. Kubota, K. Domen, *Adv. Mater.* **2013**, 25, 125.
- [7] Y. Park, K. J. McDonald, K. S. Choi, *Chem. Soc. Rev.* **2013**, 42, 2321.
- [8] F. F. Abdi, T. J. Savenije, M. M. May, B. Dam, R. van de Krol, *J. Phys. Chem. Lett.* **2013**, 4, 2752.
- [9] W. A. Smith, I. D. Sharp, N.C. Strandwitz, J. Bisquert, *Energy Environ. Sci.* **2015**, 8, 2851.
- [10] F. F. Abdi, L. Han, A. H. M. Smets, M. Zeman, B. Dam, R. V. D. Krol, *Nat. Commun.* **2013**, 4, 2195.
- [11] Y. Pihosh, I. Turkevych, K. Mawatari, J. Uemura, Y. Kazoe, S. Kosar, K. Makita, T. Sugaya, T. Matsui, D. Fujita, M. Tosa, M. Kondo, T. Kitamori, *Sci. Rep.* **2015**, 5, 11141.
- [12] K. Ye, Z. Wang, J. Gu, S. Xiao, Y. Yuan, Y. Zhu, Y. Zhang, W. Mai, S. Yang, *Energy Environ. Sci.* **2017**, 10, 772.
- [13] T. W. Kim, Y. Ping, G. A. Galli, K. S. Choi, *Nat. Commun.* **2016**, 6, 8769.
- [14] J. K. Kim, X. Shi, M. J. Jeong, J. Park, H. S. Han, S. H. Kim, Y. Guo, T. F. Heinz, S. Fan, C. Lee, J. H. Park, X. Zheng, *Adv. Energy Mater.* **2018**, 8, 1701765.
- [15] W. Liu, H. Liu, L. Dang, H. Zhang, X. Wu, B. Yang, Z. Li, X. Zhang, L. Lei, S. Jin, *Adv. Funct. Mater.* **2017**, 27, 1603904.
- [16] S. Ye, R. Chen, Y. Xu, F. Fan, P. Du, F. Zhang, X. Zong, T. Chen, Y. Qi, P. Chen, Z. Chen, C. Li, *J. Catal.* **2016**, 338, 168.
- [17] S. K. Pilli, T. E. Furtak, L. D. Brown, T. G. Deutsch, J. A. Turner, A. M. Herring, *Energy Environ. Sci.* **2011**, 4, 5028.
- [18] T. W. Kim, K. S. Choi, *Science* **2014**, 343, 990.
- [19] T. Palaniselvam, L. Shi, G. Mettela, D. H. Anjum, R. Li, K. P. Katuri, P. E. Saikaly, P. Wang, *Adv. Mater. Interfaces* **2017**, 4, 1700540.
- [20] S. Wang, T. W. He, J. H. Yun, Y. Hu, M. Xiao, A. Du, L. Wang, *Adv. Funct. Mater.* **2018**, 28, 1802685.
- [21] M. Zhong, T. Hisatomi, Y. Kuang, J. Zhao, M. Liu, A. Iwase, Q. Jia, H. Nishiyama, T. Minegishi, M. Nakabayashi, N. Shibata, R. Niishiro, C. Katayama, H. Shibano, M. Katayama, A. Kudo, T. Yamada, K. Domen, *J. Am. Chem. Soc.* **2015**, 137, 5053.
- [22] K. Zhang, B. Jin, C. Park, Y. Cho, X. Song, X. Shi, S. Zhang, W. Kim, H. Zeng, J. H. Park, *Nat. Commun.* **2019**, 10, 2001.
- [23] G. Liu, J. Shi, F. Zhang, Z. Chen, J. Han, C. Ding, S. Chen, Z. Wang, H. Han, C. Li, *Angew. Chem.* **2014**, 126, 7423.
- [24] X. Chang, T. Wang, P. Zhang, J. Zhang, A. Li, J. Gong, *J. Am. Chem. Soc.* **2015**, 137, 8356.
- [25] X. Zhao, W. Luo, J. Feng, M. Li, Z. Li, T. Yu, Z. Zou, *Adv. Energy Mater.* **2014**, 4, 1301785.
- [26] A. J. Rettie, H. C. Lee, L. G. Marshall, J. F. Lin, C. Capan, J. Lindemuth, J. S. McCloy, J. Zhou, A. J. Bard, C. B. Mullins, *J. Am. Chem. Soc.* **2013**, 35, 11389.
- [27] M. Gong, Y. Li, H. Wang, Y. Liang, J. Z. Wu, J. Zhou, J. Wang, T. Regier, F. Wei, H. Dai, *J. Am. Chem. Soc.* **2013**, 135, 8452.
- [28] J. Nai, H. Yin, T. You, L. Zheng, J. Zhang, P. Wang, Z. Jin, Y. Tian, J. Liu, Z. Tang, *Adv. Energy Mater.* **2015**, 5, 1401880.
- [29] W. He, R. Wang, L. Zhang, J. Zhu, X. Xiang, F. Li, *J. Mater. Chem. A* **2015**, 3, 17977.
- [30] T. Yao, R. Chen, J. Li, J. Han, W. Qin, H. Wang, J. Shi, F. Fan, C. Li, *J. Am. Chem. Soc.* **2016**, 138, 13664.